



Simulations of Janus droplets at equilibrium and in shear

Orest Shardt, J. J. Derksen, and Sushanta K. Mitra

Citation: *Physics of Fluids* (1994-present) **26**, 012104 (2014); doi: 10.1063/1.4861717

View online: <http://dx.doi.org/10.1063/1.4861717>

View Table of Contents: <http://scitation.aip.org/content/aip/journal/pof2/26/1?ver=pdfcov>

Published by the AIP Publishing



Re-register for Table of Content Alerts

Create a profile.



Sign up today!



Simulations of Janus droplets at equilibrium and in shear

Orest Shardt,^{1,a)} J. J. Derkens,^{1,b)} and Sushanta K. Mitra^{2,c)}

¹*Department of Chemical and Materials Engineering, University of Alberta, Edmonton, Alberta T6G 2V4, Canada*

²*Department of Mechanical Engineering, University of Alberta, Edmonton, Alberta T6G 2G8, Canada*

(Received 15 April 2013; accepted 26 December 2013; published online 15 January 2014)

Janus droplets are compound droplets that consist of two adhering drops of different fluids that are suspended in a third fluid. We use the Shan-Chen lattice Boltzmann method for multicomponent mixtures to simulate Janus droplets at rest and in shear. In this simulation model, interfacial tensions are not known *a priori* from the model parameters and must be determined using numerical experiments. We show that interfacial tensions obtained with the Young-Laplace law are consistent with those measured from the equilibrium geometry. The regimes of adhering, separated, and engulfing droplets were explored. Two different adhesion geometries were considered for two-dimensional simulations of Janus droplets in shear. The first geometry resembles two adhering circles with small overlap. In the second geometry, the two halves are semicircular. For both geometries, the rotation rate of the droplet depends on its orientation. The width of the periodic simulation domain also affects the rotation rate of both droplet types up to an aspect ratio of 6:1 (width:height). While the droplets with the first geometry oscillated about the middle of the domain, the droplets of the second geometry did not translate while rotating. A four-pole vortex structure inside droplets of the second geometry was found. These simulations of single Janus droplets reveal complex behaviour that implies a rich range of possibilities for the rheology of Janus emulsions. © 2014 AIP Publishing LLC. [<http://dx.doi.org/10.1063/1.4861717>]

I. INTRODUCTION

Simulation methods are available for studying the various industrial processes that involve flows of three fluids. While many applications involve a gas phase and two liquid phases, such as oil recovery from porous media (simulations of two-phase imbibition were described by Gunde *et al.*¹) and bubbly flows relevant to nuclear safety,² dispersions of two immiscible liquids in a third liquid have been studied only recently. These new examples of three-component systems motivate a detailed analysis of their behaviour and the evaluation of simulation methods specifically for their unique characteristics. Under certain conditions, droplets of the two dispersed liquids may adhere to form a compound droplet called a Janus droplet after the two-faced character in Roman mythology.^{3,4}

Several interesting phenomena involving Janus droplets have been recently discussed in the literature. Hasinovic *et al.* described a method for generating bulk quantities of an emulsion with Janus droplets, called a Janus emulsion.^{5,6} Adhering, engulfed, and distinct droplets have been produced in microfluidic devices.^{7,8} Droplet adhesion was also considered by Chen *et al.*,⁹ who used a third immiscible liquid to separate droplets for microfluidic protein crystallization. Finally, Guzowski *et al.*¹⁰ recently produced long Janus droplet chains in a microfluidic device. These chains are long sequences of adhering fluid drops of alternating compositions. Such chains can coil up

^{a)}Author to whom correspondence should be addressed. Electronic mail: shardt@ualberta.ca

^{b)}Electronic mail: jos@ualberta.ca

^{c)}Electronic mail: sushanta.mitra@ualberta.ca

without coalescing and could create a fluid with interesting rheology.¹⁰ Considering the range of possible geometries for a Janus droplet, emulsions of Janus droplets and chains likely have complex rheologies that depend on the interfacial tensions between the liquids. Simulations provide a way to investigate the behaviour of Janus emulsions, starting with simulations of one droplet.

Simulations of three-component systems have been previously performed using the Cahn-Hilliard model^{2,11} and the free-energy lattice Boltzmann method (LBM).¹² However, these methods were evaluated for lenses at the interface between two stratified fluids and not adhering droplets. Lenses between two stratified fluids have also been studied by Leclaire, Reggio, and Trépanier,¹³ who used the colour-model LBM. Another simulation method, the multicomponent LBM of Shan and Chen,¹⁴ has not been evaluated for lenses or adhering droplets. Hence, the focus of the present work is to evaluate the Shan-Chen method specifically for its ability to simulate Janus droplets. Though phase separation is automatic in the Shan-Chen LBM, a disadvantage of the method is that interfacial tensions are not input parameters and a theoretical equation that relates interfacial tensions to input parameters is not available.¹⁵ Therefore, interfacial tensions must be determined “empirically” from simulations by applying the Young-Laplace law to droplet interfaces and their pressure jumps. Since interfacial tensions specify the equilibrium geometry of adhering droplets, we derive equations for calculating interfacial tensions from the equilibrium geometry. We show that the Young-Laplace law and the equilibrium geometry provide consistent results for the interfacial tensions when using the Shan-Chen LBM to simulate Janus droplets. We then study the rotation of individual Janus droplets in shear flow, as observed experimentally by Torza and Mason,¹⁶ as a first step towards gaining insight into the rheology of Janus emulsions and chains.¹⁰

II. EQUILIBRIUM DROPLET GEOMETRY

The equilibrium geometry of adhering droplets was analyzed by Torza and Mason in a paper published in 1970.¹⁶ However, they did not use the nomenclature of “Janus droplet” or “Janus emulsion” and their work is rarely cited in the literature on these more recent topics. Due to the importance of the equilibrium geometry for analyzing simulations, we briefly review this topic. We also derive convenient explicit equations for measuring interfacial tensions from the equilibrium geometry and for the inverse problem of determining the geometry for known interfacial tensions. The equations could be used, for example, to measure changes in interfacial tensions over time due to diffusion of the three components and their non-zero solubilities in each other.⁹

The geometry of a pair of adhering droplets is shown in Fig. 1. For the analysis that follows, we consider a cross sectional plane through the centres of the spherical droplets. The analysis is therefore two dimensional, but results are provided for the full three-dimensional geometry as well. The bulk fluid is denoted Fluid 0. The upper droplet consists of Fluid 1, R_1 is the primary radius of curvature, and the angle between the centre line and the three fluid contact point is θ_1 . The definitions are the same for the lower droplet of Fluid 2, but a subscript 2 replaces the 1. The radius of curvature of the interface between the droplets is R_c . Without loss of generality, the lower droplet is assumed to have a higher internal pressure P_2 than the upper droplet (with pressure P_1). The interfacial tension between fluids i and j is denoted γ_{ij} .

As in Torza and Mason,¹⁶ a force balance between the interfacial tensions is used to study the equilibrium geometry. Figure 2 shows the geometry of the interfacial forces. The horizontal force balance is

$$\gamma_{01} \cos(\theta_1) + \gamma_{02} \cos(\theta_2) = \gamma_{12} \cos(\theta_c). \quad (1)$$

The vertical force balance is

$$\gamma_{01} \sin(\theta_1) + \gamma_{12} \sin(\theta_c) = \gamma_{02} \sin(\theta_2). \quad (2)$$

Since the co-linear circles defined by the radii R_1 , R_2 , and R_c all intersect at the three fluid contact point, we have the condition that

$$a \equiv R_1 \sin(\theta_1) = R_2 \sin(\theta_2) = R_c \sin(\theta_c). \quad (3)$$

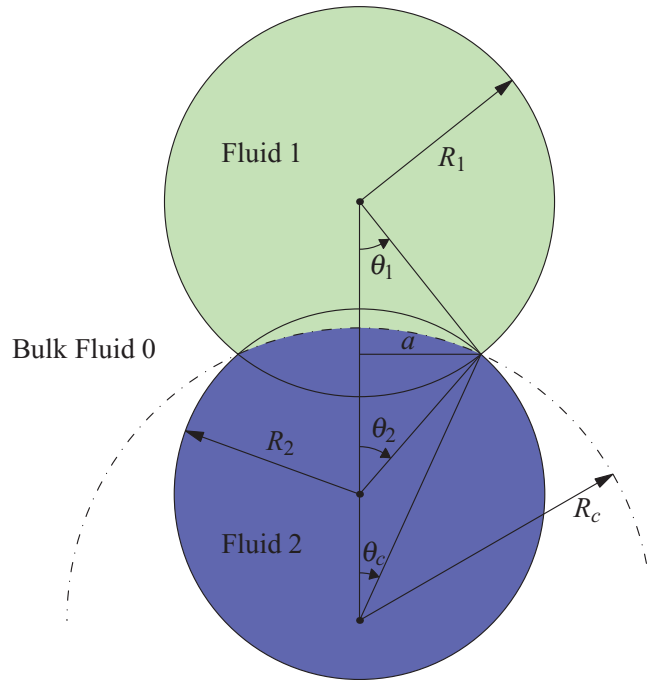


FIG. 1. Geometry of a cross section through a pair of adhering droplets.

Substitution of Eq. (3) into Eq. (2) provides

$$\frac{\gamma_{01}}{R_1} + \frac{\gamma_{12}}{R_c} = \frac{\gamma_{02}}{R_2}. \quad (4)$$

The vertical force balance is therefore equivalent to the Young-Laplace law condition that the pressure jump across one droplet-bulk interface must be the sum of the pressure jumps across the

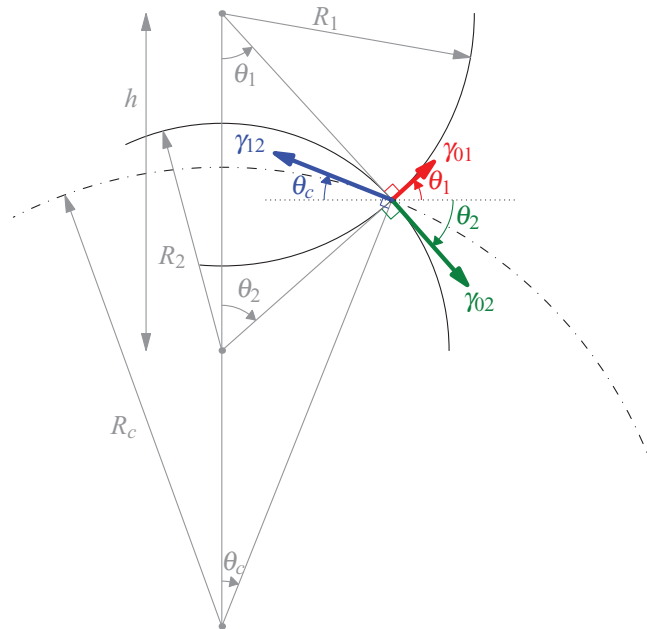


FIG. 2. Force balance at the three fluid contact point between two adhering droplets.

other droplet-bulk interface and the droplet-droplet interface. That is,

$$P_2 - P_0 = (P_2 - P_1) + (P_1 - P_0) \Rightarrow \frac{2\gamma_{02}}{R_2} = \frac{2\gamma_{12}}{R_c} + \frac{2\gamma_{01}}{R_1}. \quad (5)$$

Here we have used the Young-Laplace law for the pressure jump ΔP across a droplet interface with radius R and surface tension γ , which is

$$\Delta P = \alpha \frac{\gamma}{R}, \quad (6)$$

where $\alpha = 1$ for a circle in 2D and $\alpha = 2$ for a sphere in 3D.

Interfacial tensions and droplet volumes can be determined from measurements of the equilibrium geometry. Using Eqs. (1) and (4), the ratios of the interfacial tensions as a function of the angles and radii are

$$\frac{\gamma_{01}}{\gamma_{12}} = \frac{R_1}{R_c} \left(\frac{R_c \cos(\theta_c) - R_2 \cos(\theta_2)}{R_1 \cos(\theta_1) + R_2 \cos(\theta_2)} \right), \quad (7)$$

$$\frac{\gamma_{02}}{\gamma_{12}} = \frac{R_2}{R_c} \left(\frac{R_c \cos(\theta_c) + R_1 \cos(\theta_1)}{R_1 \cos(\theta_1) + R_2 \cos(\theta_2)} \right). \quad (8)$$

Alternatively, using Eqs. (1) and (2), the ratios as a function of only the angles are

$$\frac{\gamma_{01}}{\gamma_{12}} = \frac{\sin(\theta_2) \cos(\theta_c) - \cos(\theta_2) \sin(\theta_c)}{\cos(\theta_1) \sin(\theta_2) + \cos(\theta_2) \sin(\theta_1)}, \quad (9)$$

$$\frac{\gamma_{02}}{\gamma_{12}} = \frac{\cos(\theta_1) \sin(\theta_c) + \sin(\theta_1) \cos(\theta_c)}{\cos(\theta_1) \sin(\theta_2) + \cos(\theta_2) \sin(\theta_1)}. \quad (10)$$

The individual interfacial tensions cannot be determined because the force balance would be satisfied without a change in geometry if all interfacial tensions were to be scaled by the same factor.

For completeness, we provide equations for calculating the cross-sectional areas of the droplets and their volumes. The droplet cross-sectional areas for the geometry shown in Fig. 1 are

$$A_1 = \pi R_1^2 - \frac{1}{2} R_1^2 (2\theta_1 - \sin(2\theta_1)) - \frac{1}{2} R_c^2 (2\theta_c - \sin(2\theta_c)), \quad (11)$$

$$A_2 = \pi R_2^2 - \frac{1}{2} R_2^2 (2\theta_2 - \sin(2\theta_2)) + \frac{1}{2} R_c^2 (2\theta_c - \sin(2\theta_c)). \quad (12)$$

The droplet volumes are

$$V_1 = \frac{4}{3} \pi R_1^3 - \frac{\pi R_1^3}{3} (2 - 2 \cos \theta_1 - \cos \theta_1 \sin^2 \theta_1) - \frac{\pi R_c^3}{3} (2 - 2 \cos \theta_c - \cos \theta_c \sin^2 \theta_c), \quad (13)$$

$$V_2 = \frac{4}{3} \pi R_2^3 - \frac{\pi R_2^3}{3} (2 - 2 \cos \theta_2 - \cos \theta_2 \sin^2 \theta_2) + \frac{\pi R_c^3}{3} (2 - 2 \cos \theta_c - \cos \theta_c \sin^2 \theta_c). \quad (14)$$

Determining the equilibrium geometry explicitly for given interfacial tensions (γ_{01} , γ_{02} , and γ_{12}) and droplet sizes (R_1 and R_2) is more complex. The required angles, inter-droplet distance, and internal interface curvature are

$$\theta_1 + \theta_2 = \cos^{-1} \left[\frac{1}{2} \frac{1 - \left(\left(\frac{\gamma_{01}}{\gamma_{12}} \right)^2 + \left(\frac{\gamma_{02}}{\gamma_{12}} \right)^2 \right)}{\left(\frac{\gamma_{01}}{\gamma_{12}} \right) \left(\frac{\gamma_{02}}{\gamma_{12}} \right)} \right], \quad (15)$$

$$h^2 = R_1^2 + R_2^2 + 2R_1R_2 \cos(\theta_1 + \theta_2), \quad (16)$$

$$\theta_1 = \cos^{-1} \left[\frac{R_1^2 + h^2 - R_2^2}{2R_1h} \right] = \cos^{-1} \left[\frac{R_1 + R_2 \cos(\theta_1 + \theta_2)}{h} \right], \quad (17)$$

$$\theta_2 = \cos^{-1} \left[\frac{R_2^2 + h^2 - R_1^2}{2R_2h} \right] = \cos^{-1} \left[\frac{R_2 + R_1 \cos(\theta_1 + \theta_2)}{h} \right], \quad (18)$$

$$\theta_c = -\theta_1 + \cos^{-1} \left[\frac{1}{2} \frac{-1 + \left(\left(\frac{\gamma_{01}}{\gamma_{02}} \right)^2 + \left(\frac{\gamma_{12}}{\gamma_{02}} \right)^2 \right)}{\left(\frac{\gamma_{01}}{\gamma_{02}} \right) \left(\frac{\gamma_{12}}{\gamma_{02}} \right)} \right], \quad (19)$$

$$\frac{1}{R_c} = \frac{1}{R_2} \frac{\gamma_{02}}{\gamma_{12}} - \frac{1}{R_1} \frac{\gamma_{01}}{\gamma_{12}}. \quad (20)$$

The radii can be related to the areas using Eqs. (11) and (12); the volumes are specified by Eqs. (13) and (14).

When ensuring that the arguments of \cos^{-1} are bounded between ± 1 , we obtain the same conditions as Chen *et al.*⁹ for equilibrium adhesion of droplets:

$$\gamma_{01} \leq \gamma_{02} + \gamma_{12}, \quad (21)$$

$$\gamma_{02} \leq \gamma_{01} + \gamma_{12}, \quad (22)$$

$$\gamma_{12} \leq \gamma_{01} + \gamma_{02}. \quad (23)$$

If these conditions are not satisfied, the interfacial tensions cannot balance and the droplets will remain separated (when $\gamma_{12} > \gamma_{01} + \gamma_{02}$) or one will engulf the other (when $\gamma_{01} > \gamma_{02} + \gamma_{12}$ or $\gamma_{02} > \gamma_{01} + \gamma_{12}$). An interesting observation is that the conditions for adhesion depend only on the interfacial tensions; the relative sizes of the droplets do not affect the outcome of droplet interactions. This explains why adhering droplets with a wide range of diameters were produced by the bulk emulsification method of Hasinovic, Friberg, and Rong.⁵ Another consequence of the adhesion conditions is that for a given set of three fluids, changing which phase is the continuous phase can turn a system with engulfing droplets into one with distinct droplets or vice versa. If droplets adhere for one choice of dispersed and continuous phases, the dispersed phase droplets will adhere for all choices.

The special case of a flat interface between adhering droplets must be considered separately. The condition for a flat interface is

$$\frac{\gamma_{01}}{R_1} = \frac{\gamma_{02}}{R_2}. \quad (24)$$

When this condition is satisfied, $R_c \rightarrow \infty$ and the pressures in the droplets are equal.

We now apply the results of the geometric analysis to determine interfacial tensions in three-component Shan-Chen LBM simulations. We verify that the correct equilibrium geometry is obtained.

III. SIMULATION METHOD

Systems with multiple immiscible fluids can be simulated using the multicomponent lattice Boltzmann method of Shan and Chen.¹⁴ In this model, multiple fluids are coupled through a repulsive interaction potential that maintains phase separation and provides interfacial tension. For simplicity, two-dimensional simulations were used to study droplet interactions. A regular lattice with nine discrete directions was used (a D2Q9 lattice). For brevity, the details of the lattice Boltzmann

TABLE I. Input parameters for the six simulations.

Case	g_{01}	g_{02}	g_{12}	R_1	R_2
1	0.30	0.25	0.20	45	45
2	0.23	0.33	0.27	45	45
3	0.30	0.30	0.15	45	45
4	0.26	0.24	0.31	45	27
5	0.17	0.17	0.40	45	30
6	0.15	0.38	0.15	45	30

method and Shan-Chen multicomponent model are omitted here. Chen and Doolen¹⁷ and Aidun and Clausen¹⁸ provide a review of lattice Boltzmann methods, the multicomponent model is described by Shan and Chen¹⁴ and Shan and Doolen,¹⁹ and examples of applications are provided by Yang *et al.*²⁰ and Kang, Zhang, and Chen.¹⁵ We used a single-relaxation-time BGK (Bhatnagar-Gross-Krook) collision operator with equal relaxation times for each component of the multicomponent Shan-Chen model. Since separation of the components into liquid and vapour phases is undesirable, each component was treated as ideal. The interaction forces between components were implemented by shifting the velocity used in the calculation of the equilibrium density distribution.

The magnitudes of the repulsive interactions between each pair of fluids are inputs into the Shan-Chen model. The effect of the interaction potential strength on interfacial tension must be determined empirically.^{15,20} This is performed by measuring the interfacial curvature and the pressure difference from simulation data and applying the Young-Laplace law. Pressures in LBM simulations are obtained using an equation of state. For the multicomponent model, the equation of state for the pressure P at each lattice node is^{15,19,20}

$$P = \frac{1}{3} \sum_k \rho_k + \frac{3}{2} \sum_{k,\bar{k}} g_{k\bar{k}} \rho_k \rho_{\bar{k}}, \quad (25)$$

where g_{ij} is the interaction potential strength between fluids i and j , k counts over the number of components, and ρ_k is the density of the k th component. The notation \bar{k} denotes the values of the index that differ from k . The factor of $\frac{3}{2}$ arises from the projection of a four dimensional face-centred hypercubic (FCHC) lattice to two dimensions. Due to this projection, the interaction strengths along the directions of the lattice have different weights. Like the weighting used by Kang, Zhang, and Chen¹⁵ for a three-dimensional simulation, we use g_{ij} for the directions with length 1 and $\frac{1}{4}g_{ij}$ for the directions with length $\sqrt{2}$. The values of g_{ij} used in this work are between 0.15 and 0.4 (Table I), ensuring that the components remain separated and the simulations are stable.

IV. RESULTS AND DISCUSSION

A. Equilibrium configurations

Table I lists the parameters for the six runs that were used to study equilibrium configurations. In all cases, the domain was fully periodic with 256×256 nodes, chosen to ensure adequate resolution of the droplets. For each case, the domain was initialized with two circular droplets of Fluids 1 and 2 in Fluid 0. To ensure slight overlap and therefore interaction between the droplets, the distance between the centres of the circles was 98% of the sum of their radii. The density of each fluid was initialized as 1 where that fluid is present and 0.01 in the remainder of the domain. The relaxation times of all three fluids were one, corresponding to a kinematic viscosity of $\frac{1}{6}$. These values are given in lattice units, with the lattice spacing (length scale), time step (time scale), and reference mass (density scale) all being one.

Figure 3 shows the simulation state for each case after 500 000 time steps, which was found to be sufficient to achieve steady state in all cases. The circles shown in Fig. 3 were determined by fitting circles to points on the interface between each pair of fluids. The interface between fluids i and j was considered to be located where the densities of the two fluids were equal as determined

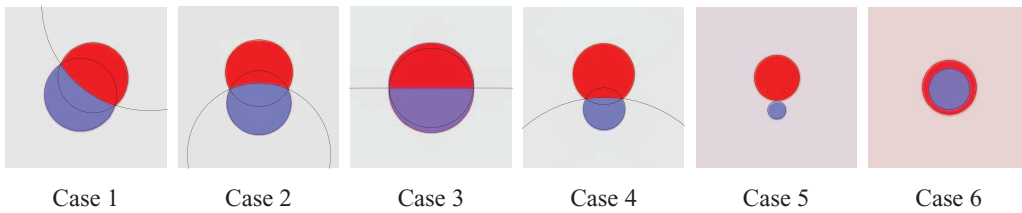


FIG. 3. Equilibrium droplet shapes for Cases 1–6 with circles fitted to the interfaces.

using linear interpolation between nodal values. The centres and radii of the circles were obtained using the least-squares fitting method of Pratt.²¹ This method was chosen due to its robustness when fitting circles with a large radius to data from a small arc such as the interface between two droplets. While the droplets adhere in Cases 1–4, they remain separate in Case 5, and one engulfs the other in Case 6.

Figure 4 shows the evolution of the Case 2 simulation from the initial condition towards equilibrium. After the upper fluid spreads over the lower droplet, it retracts slightly before reaching the equilibrium shape.

We can obtain the interfacial tensions from the Young-Laplace law by using the radii of the fitted circles and the pressures in each fluid phase. The dependence of the interfacial tension, which was measured in this way, on the strength of the interaction potential is shown in Fig. 5. Since the fluid interface is absent for one fluid pair in Cases 5 and 6, the interfacial tensions between those pairs of fluids cannot be obtained by applying the Young-Laplace law. The Young-Laplace law also cannot be used for Case 3 because the interface between the two droplet phases is flat and the pressure difference vanishes. The interfacial tensions can, however, be estimated using a linear least-squares fit to the data in Fig. 5. We note that the horizontal axis intercept at $g_{ij} = 0.085$ reflects the fact that the interaction potential strength must exceed a threshold for phase separation to occur. For Case 5, the tension of the interface that is absent at equilibrium is estimated as 0.14; in Case 6, it is 0.13. In both of these cases, the tension of the absent interface exceeds the sum of the tensions of the present interfaces, preventing adhesion of the droplets. In the other cases (1–4), the maximum tension is less than the sum of the others, and we obtain adhering droplets. In Case 3, the tension of the flat interface γ_{12} is estimated to be 0.03, which is about one third of the other two interfacial tensions (0.08), creating the nearly semicircular shape of both droplet phases. The simulation results are therefore consistent with the adhesion conditions, Eqs. (21)–(23).

The interfacial tension ratios determined from the equilibrium geometry are compared with the ratios of the Young-Laplace interfacial tensions in Fig. 6. Only the cases in which all three tensions could be determined from the Young-Laplace law are considered, i.e., 1, 2, and 4. The excellent agreement throughout the range of tested ratios indicates that the Shan-Chen LBM for simulating ternary mixtures of immiscible fluids reproduces the expected interfacial force behaviour. The relative differences between the ratios computed using Eqs. (7) and (8) (shown in Fig. 6) versus (9) and (10) were below 0.2%. The equivalence of the two sets of equations for the tension ratios depends on the geometry satisfying the mutual contact constraint given by Eq. (3). The close agreement between

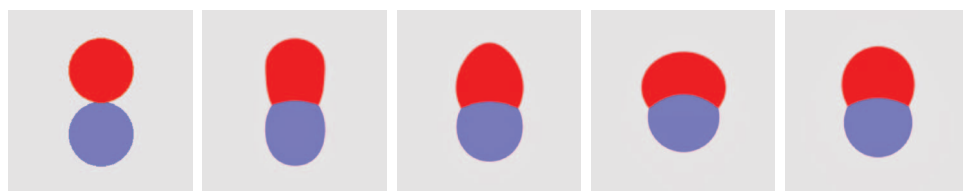


FIG. 4. Initial droplet shapes followed by the shapes after 1000, 2000, 5000, and 10 000 time steps (left to right) for Case 2. See the accompanying video for an animation (Multimedia view). [URL: <http://dx.doi.org/10.1063/1.4861717.1>]

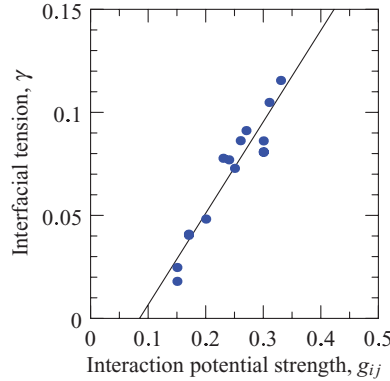


FIG. 5. Interfacial tension (in lattice units) as a function of interaction potential strength for all cases (dots) together with the least-squares linear fit (line), $\gamma = 0.444g_{ij} - 0.0377$.

the results for the two sets of equations therefore indicates that the three fitted circles all intersect at the same points.

B. Janus droplets in shear flow

The behaviour of a Janus droplet in shear, and therefore the rheology of Janus emulsions, depends on the shape of the compound drop. Torza and Mason¹⁶ studied the rotation of Janus droplets in shear experimentally, and we now consider analogous simulations. In the simulations of droplets at equilibrium, all four boundaries are periodic. In the simulations of sheared droplets that follow, the left and right boundaries remain periodic while the upper and lower boundaries are replaced with solid walls moving at a constant horizontal speed (in opposite directions). These velocity boundary conditions were applied using the method of Ladd²² to each of the three fluids. This method conserves the mass of each component. In contrast, the boundary condition of Zou and He²³ does not ensure mass conservation, causing problems with the low-concentration components along the boundaries. In simulations with the Zou and He²³ boundary condition, layers with fluid of one of the droplet components formed at the sheared walls.

While the steady-state flow field around a stationary droplet should be zero, spurious currents are present near interfaces in many multiphase fluid simulation methods due to discretization errors. In the Shan-Chen method, spurious currents are the result of discretization in density gradient calculations and a consequent lack of isotropy.²⁴ Figure 7 shows the steady-state spurious currents for Cases 2 and 3 (in Table I). The maximum spurious current magnitudes occur at the nodes along

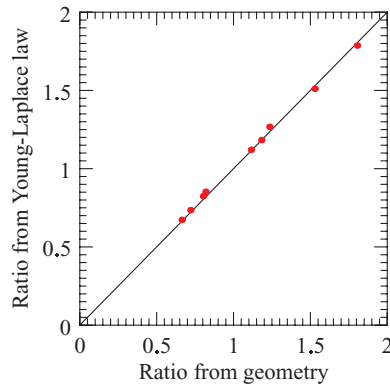


FIG. 6. Parity plot of the tension ratios obtained from the equilibrium geometry (Eqs. (7) and (8)) and the Young-Laplace law.

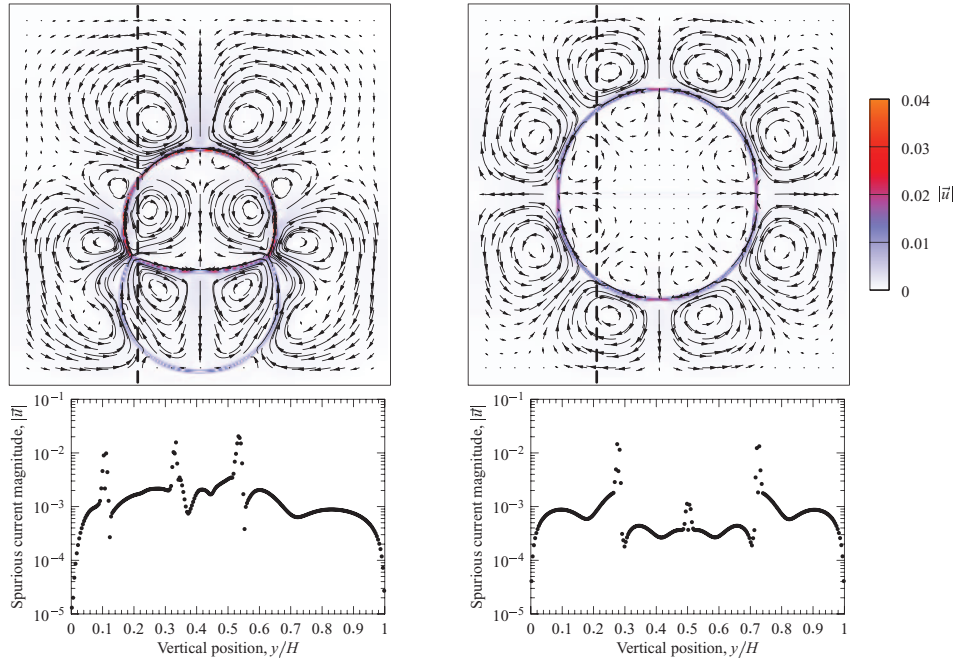


FIG. 7. Spurious currents at steady state in Cases 2 (left) and 3 (right). The maximum speed is 0.034 in Case 2 and 0.020 in Case 3. The bottom figures show the spurious current magnitudes along the dashed vertical lines in the upper figures.

the interfaces and are of order 10^{-2} . As shown in Fig. 7, the spurious currents then rapidly decrease by an order of magnitude as the distance from the interface increases. Spurious currents are typically of order 10^{-3} at nodes that are at least three nodes away from an interface. The magnitude of the spurious currents imposes a lower bound on the shear speeds that can be considered for simulations of droplets in shear. The characteristic speed $\dot{\gamma}R$, where $\dot{\gamma}$ is the shear rate and R is a characteristic radius of the compound drop, and therefore the wall shear speed must be higher than the speed of the spurious currents. Otherwise, spurious currents dominate, and unphysical results are expected. High shear rates are therefore desirable, but arbitrarily large shear rates cannot be used because flow speeds must be lower than the speed of sound in the LBM simulations ($\frac{1}{\sqrt{3}}$) to ensure that incompressible flow is simulated. Due to these constraints on the shear speed, we consider shear speeds u_0 between 0.005 and 0.05 at the walls.

The behaviour of two types of Janus droplets (Case 2 and 3) in shear was studied to show the effect of the surface tension ratios on the behaviour of one droplet in shear. Figure 8 illustrates the behaviour of a Case 2 droplet. For all the simulations of shear flow, the two initial drop radii were 45 lattice nodes. The shear flow was started instantaneously after 100 000 timesteps of equilibration. The domain size was $W \times H = 256 \times 256$. For droplets in shear flow, we can define a Reynolds number $Re = \frac{\dot{\gamma}L^2}{\nu}$, where $\dot{\gamma} = \frac{2u_0}{H}$ is the shear rate, L is a characteristic length, and ν is a kinematic viscosity (all three fluids have $\nu = \frac{1}{6}$). The ratio of viscous and capillary forces is described by

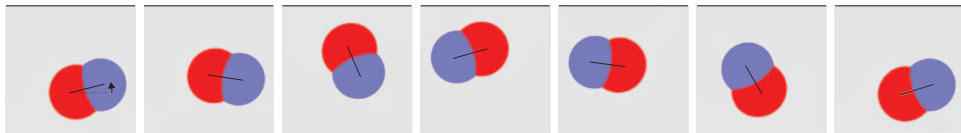


FIG. 8. Janus droplet in shear at $Re = 0.95$. A solid line connects the centres of mass of the two adhering droplets. The view shifts horizontally with the centre of mass of the red drop. The definition of the orientation angle ϕ is shown in the first frame. Time proceeds from left to right, and the dimensionless time interval between each frame is $\dot{\gamma}t = 3.9$. See the accompanying video for an animation (Multimedia view). [URL: <http://dx.doi.org/10.1063/1.4861717.2>]

a capillary number $\text{Ca} = \frac{\mu\dot{\gamma}L}{\gamma}$, where μ is a dynamic viscosity and γ is an interfacial tension. In a system with three fluids and three fluid-fluid interfaces, there are many choices for specifying the capillary number. For the simulations with fixed fluid properties and varying shear rates, it is convenient to define another dimensionless parameter: the ratio of the Reynolds and capillary numbers $\frac{\text{Re}}{\text{Ca}} = \frac{\gamma L}{\rho v^2}$. This parameter does not depend on the shear rate and contains only geometric and fluid parameters. Using the initial droplet radius (45) as the characteristic length, a fluid density of one, and a typical droplet-bulk interfacial tension of 0.1 (density and tension are in lattice units), we obtain $\frac{\text{Re}}{\text{Ca}} = 162$. With the initial radius of the droplets (45) as the characteristic length and shear speeds between 0.005 and 0.05, the range of Reynolds numbers is 0.47 and 4.7. For such Reynolds numbers of order 1, capillary numbers are of order 10^{-2} , which indicates that little deformation from a circular interface shape should be expected due to the dominance of interfacial forces over viscous stresses. The absence of noticeable deformation from the equilibrium shape is confirmed in Fig. 8.

The rotation rate of a Janus droplet and the vertical component of its centre of mass at two shear rates (Reynolds numbers) are shown in Fig. 9 for one rotation cycle. For $\text{Re} \ll 1$, rigid spherical droplets²⁵ and cylinders in shear²⁶ rotate at an average angular rate $\omega = \frac{1}{2}\dot{\gamma}$. The speed of a point on the interface of a droplet depends on its position along the interface,^{25,27} and the rotation rate of a pair of spheres depends on its angle relative to the flow.²⁸ We therefore show the dimensionless rotation rate $\frac{2\omega}{\dot{\gamma}}$ as a function of the orientation angle ϕ . The orientation of the Janus droplets was determined by finding the centres of mass of the two constituent droplets. The angle ϕ is the angle between the horizontal axis and the line connecting the centres of mass (this line segment is shown in Fig. 8). Rotation rates were obtained using central finite differences. In the two cases, the rotation rates vary around an average of about $\bar{\omega} = 0.35\dot{\gamma}$ with an amplitude of $0.25\dot{\gamma}$. The rotation rates are lowest when the droplet is horizontal, i.e., $\phi \approx 0$; rotation is fastest when $\phi \approx \pi/2$ and the droplet is oriented vertically. The rotation rates are nearly the same for the two Reynolds numbers. Despite the subtle asymmetry in the shape of the Janus droplet, the rotation rate exhibits a periodicity with a period of π with respect to the orientation angle. The vertical motion, however, repeats over a period of 2π . At both Reynolds numbers, the Janus droplet is closest to either wall when the larger radius (red) portion of the droplet is closer to the wall and the droplet is oriented with the shear flow (i.e., $0 < \phi < \pi/2$ or $-\pi < \phi < -\pi/2$). The amplitude of the vertical motion decreases slightly with increasing Reynolds number. This trend of decreasing amplitude in the vertical motion continues to higher Reynolds numbers; in a simulation with $\text{Re} = 4.7$, the droplet did not rotate or move vertically, but instead adopted a steady orientation and vertical position. The changes in behaviour may be due to the increasing effects of confinement and the finite size of the periodic domain with increasing Reynolds numbers. Simulations with larger domains are needed to assess these effects. However, such studies are not currently possible due to the restricted range of parameters in which simulations are feasible. Maintaining the same Re and droplet radius while increasing the domain size by a factor of two (while keeping the relaxation time equal to one for low spurious currents) requires increasing the shear speed by the same factor, making it approach the speed of sound in the LBM.

Simulations in wider domains are possible, and Fig. 9 shows the effects of increasing the width of the domain on the motion of a Case 2 Janus droplet sheared at $\text{Re} = 0.95$. The size of droplets in these simulations with the Shan-Chen method is the result of an equilibrium between the droplet and bulk concentrations, and therefore the initial concentrations of the droplet components in the bulk (see Sec. IV A) must be changed as the domain size is increased to ensure that the equilibrium droplet size remains constant. Several simulations were performed to find the required initial concentrations of the two phases in the larger domains that would provide the same drop size as in the smallest domain. Though varying one concentration affects the size of both adhering drops, the effect on the drop of the phase that is not varied is significantly smaller than the effect on the drop of the phase that is varied. Consequently, the two unknown initial concentrations may be determined by independently varying them until the sizes of both drops are correct. In the widest domain, the required drop sizes could not be achieved only by varying the bulk concentration of the drop phases, and therefore the initial concentration in the drop phase was also varied. Keeping all other parameters constant, increasing the width of the domain alters the rotation and translation of the droplets. The

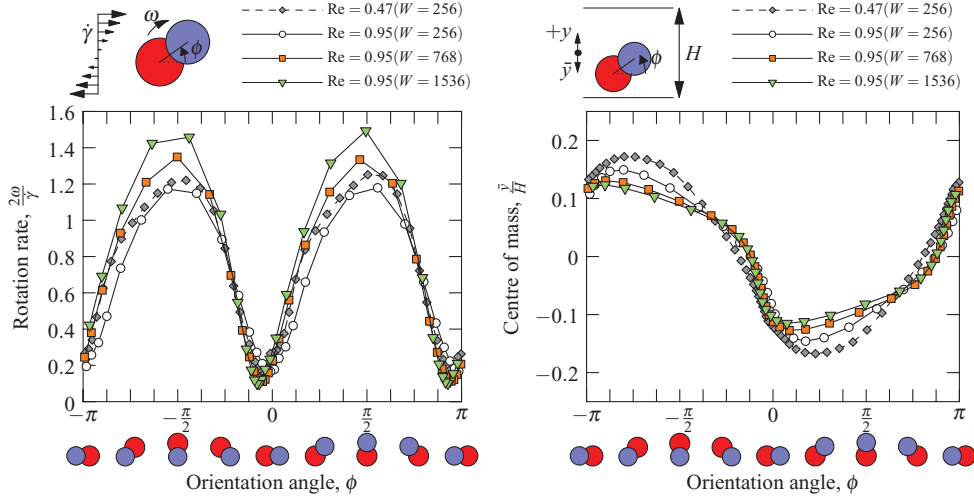


FIG. 9. Non-dimensional rotation rate (left) of a Case 2 Janus droplet and the vertical component of the centre of mass (right) as a function of the orientation angle at two Reynolds numbers and several domain widths at $Re = 0.95$. Due to the definition of ϕ , time proceeds from right to left (π to $-\pi$).

effect of the domain width on the vertical motion is small: the amplitude of the vertical oscillation decreases 19% as the width of the domain increases by a factor of six. Over this six-fold increase in width, the orientations for minimum and maximum rotation rate remain effectively constant, the minimum rotation rate decreases slightly, and the maximum rotation rate increases. The result is a net increase in the average rotation rate from $\bar{\omega} = 0.35\dot{\gamma}$ to $0.4\dot{\gamma}$. The amplitude of the variation in the rotation rate increases from $0.25\dot{\gamma}$ to $0.35\dot{\gamma}$.

For comparison with the Case 2 simulations, the experimental rotation rates obtained for a similar Janus droplet geometry by Torza and Mason¹⁶ are shown in Fig. 10. The data for the two shear rates collapse to a single curve with an average rotation rate $\bar{\omega} = 0.5\dot{\gamma}$ and an amplitude of $0.2\dot{\gamma}$. Torza and Mason¹⁶ also measured the periods τ of the rotation, obtaining values of $\dot{\gamma}\tau/4\pi$ between 1.09 and 1.26. In the simulations (Fig. 9), the periods are $\dot{\gamma}\tau/4\pi \approx 1.8$ for both Reynolds numbers and independent of the domain width. The periods of rotation in the experiments and simulations may be compared with the period of a rigid ellipsoid with a similar aspect ratio. For a rigid ellipsoid with an axis ratio of 1.3 (a typical aspect ratio of the experimental and simulated Janus droplets), the period of a Jeffery²⁹ orbit is $\dot{\gamma}\tau/4\pi = 1.03$. The experimental droplets therefore rotate slightly slower than rigid ellipsoids and faster than the simulated droplets. In the experiments, the droplet liquids are 830 (castor oil) and 6400 (silicone oil) times more viscous (dynamic viscosity) than the external liquid (water with surfactant). All three components had similar densities. In the simulations, both

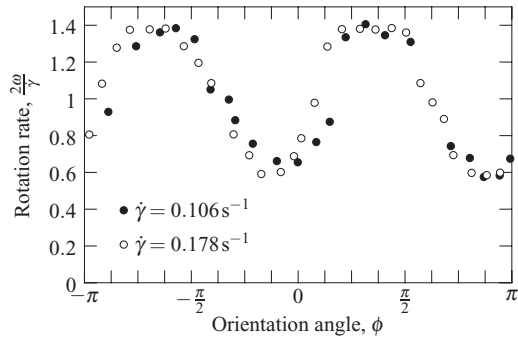


FIG. 10. Non-dimensional rotation rates of the Janus droplets studied experimentally by Torza and Mason¹⁶ at two shear rates.

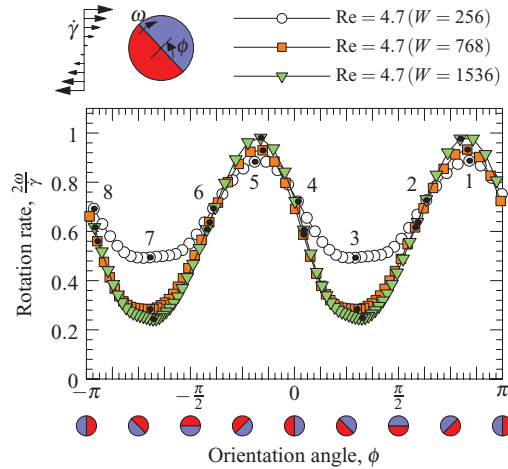


FIG. 11. Non-dimensional rotation rate of a Case 3 Janus droplet at $Re = 4.7$. Due to the definition of ϕ , time proceeds from right to left (π to $-\pi$). The time interval between consecutive symbols is constant. The filled circles and numbers indicate the positions of the frames shown in Fig. 12.

the densities and viscosities of the three liquids were nearly the same. Since the rotation rate of fluid spheres increases towards the rate of rigid particles as the viscosity of the internal fluid increases,²⁵ the difference in rotation rates between the experiments and simulations is tentatively attributed to the higher viscosity of the experimental droplets relative to the external fluid. The viscosity ratio between the two droplet fluids is also expected to affect the dynamics of Janus droplets, but the effect may be small when both droplet fluids are significantly more viscous than the external fluid and the capillary number is low, making the Janus droplet move as a rigid body through the external fluid. It should be noted that the simulations are two-dimensional and the effect of this difference between the simulations and experiments has not been evaluated. Since both rigid spheres²⁵ and cylinders²⁶ rotate at half the shear rate, the effect of dimensionality on the rotation rate might not be significant, but remains to be verified with three-dimensional simulations. Analyses of the effects of the vertical confinement are also left for future work with three-dimensional simulations.

In simulations with $Re < 0.2$, the Case 2 Janus droplet did not rotate. At these low shear rates, spurious currents become comparable in magnitude to the imposed shear flow, and the absence of rotation (unlike the low-Re experiments of Torza and Mason¹⁶) is considered an unphysical effect of the spurious currents. Results at $0.2 < Re < 0.47$ are not presented because it is unclear if the behaviour is unphysical due to the role of spurious currents.

Case 3 Janus droplets, in which the shape of the adhering droplets is nearly semicircular, behave very differently from Case 2 droplets. One significant difference is the absence of vertical motion: fluctuations in the vertical position of the centre of mass are less than half the lattice spacing. Another difference is in the dependence of the angular velocity on the orientation angle, as shown in Fig. 11. Results are shown only for $Re = 4.7$, at which spurious currents do not appear to have a significant effect. With lower Reynolds numbers (0.47, 0.95, and 1.9) the internal flow field relative to rigid rotation (as will be described in the following paragraph) resembled the eight-pole structure of the spurious currents shown in Fig. 7. At $Re = 4.7$, the rotation rate ω fluctuates around a mean of $\bar{\omega} = 0.35\dot{\gamma}$ with an amplitude of $0.1\dot{\gamma}$. Case 3 droplets therefore rotate at about the same average rate as Case 2 droplets, but the amplitude of the fluctuations is significantly lower for Case 3. Furthermore, the maximum and minimum rotation rates no longer occur when the two halves of the Janus droplet are oriented vertically or horizontally. The differences between the two cases are related to the more even distribution of mass around the centre of mass in Case 3. Unlike Case 2, the area exposed perpendicular to the flow does not change significantly as the Case 3 Janus droplet rotates, creating a weaker dependence of the rotation rate on the orientation. A better understanding of the rotation behaviour of Case 3 droplets can be obtained by studying the flow inside them.

As for the Case 2 droplets, we examine the effects of increasing the width of the domain on the behaviour of Case 3 Janus droplets. Simulations in a larger horizontal domain assist future comparison of the (two-dimensional) simulations with experiments, which have not been reported for sheared semi-circular droplets. Experiments with (homogeneous) droplets sheared in a narrow gap (only slightly larger than the diameter of the drop) have been performed,³⁰ and therefore experiments are possible with the same ratio $2R/H \approx 0.5$ as in the simulations, where R is the radius of the undeformed, semi-circular Janus droplet. Replicating a periodic domain (with a series of equally spaced drops) is not practical, but simulations in successively larger domains can be used to evaluate the effect of horizontal periodicity. Maintaining constant drop size while increasing the domain size is easier with Case 3 droplets than with Case 2 droplets because the two drop phases interact identically with the bulk phase. Only one initial concentration therefore needs to be found to keep the sizes of both drops constant. As shown in Fig. 11, the change in the rotation rate when doubling the domain size from $W = 768$ to $W = 1536$ is small, indicating that these simulations describe droplets that are not confined horizontally. Comparing the horizontally confined ($W = 256$) and unconfined ($W \geq 768$) cases, the orientations for minimum and maximum rotation speed remain the same, while the rotation speeds are different. For horizontally unconfined droplets, the maximum rotation rate increases to $0.5\dot{\gamma}$ and the minimum rate decreases from $0.25\dot{\gamma}$ to $0.14\dot{\gamma}$. The amplitude of the fluctuation in the rotation rate of unconfined droplets is therefore nearly double the amplitude of confined droplets. The period of the rotation increases from $\dot{\gamma}\tau/4\pi = 1.6$ (confined) to 2.1 (unconfined).

To gain insight into the dependence of the rotation rate on the orientation angle and the difference between the rotation of a Case 3 Janus droplet and a rigid body, we consider the motion of the fluid in the Janus droplet relative to the motion of an equivalently shaped rigid body that rotates with the same angular velocity. For each orientation ϕ shown in Fig. 12, the velocity due to rigid rotation (\vec{u}_{rot}) at a rate $\omega(\phi)$ about the centre of mass of the compound droplet was subtracted from the fluid velocity (\vec{u}). The streamlines of the resulting velocity field are shown in Fig. 12. For reference, the relative velocity field for a cross-section of an undeformed, spherical, homogeneous drop in creeping flow^{25,27,31} is shown in Fig. 13. While simulations at lower Reynolds numbers showed a pattern with eight rotation centres, the streamlines at $Re = 4.7$ clearly differ from the eight-pole spurious current structure (Fig. 7). A four-pole vortex structure can be seen in the even-numbered frames. The structure and magnitude of the relative flow are similar to those of the exact solution (Fig. 13), supporting the conclusion that the flow is not spurious. Compared to the exact solution, the structure in the deformed drop is only slightly rotated in the direction of the applied shear. The centres of the four vortices remain constant in a stationary reference frame; they do not rotate with the droplet. The upper (right of centre) and lower (left of centre) vortices circulate in the direction of the applied shear, while the left (above centre) and right (below centre) vortices rotate in the opposite direction. When the internal interface passes near two of the vortex centres, the corresponding vortices are not present. Thus, all four vortices are present in frames 2, 4, 6, and 8, while only two are clearly visible in the other orientations. The periodicity with period π in Fig. 11 indicates that the simulation results are symmetric with respect to an exchange of the two droplet fluids.

Figure 12 also shows the relative velocities in positions 5–8 for three horizontal domain sizes. Again, the differences between the simulations with $W = 768$ and $W = 1536$ are small, indicating that the results with these domain sizes represent the behaviour of a droplet that is not confined horizontally. In the two larger domains, the droplets deform more from a circular shape. Horizontal confinement reduces the amplitude of the oscillation in the rotation rate (Fig. 11) and the magnitude of the flow relative to rigid rotation, but the structure of the vortices remains generally unchanged.

The rotation rate and vortex structure depend on the orientation of the droplet in the following manner:

- *Position 1.* The droplet rotates fastest in this position. The internal interface is inclined with the applied shear direction. Two vortices are present and both rotate against the applied shear. The (absolute not relative) fluid flow in the vortex near the outer interface therefore moves slower than rigid rotation, while the flow near the centre of the Janus droplet moves faster. As the droplet rotates past position 1, the two vortices decrease in size and the rotation slows.

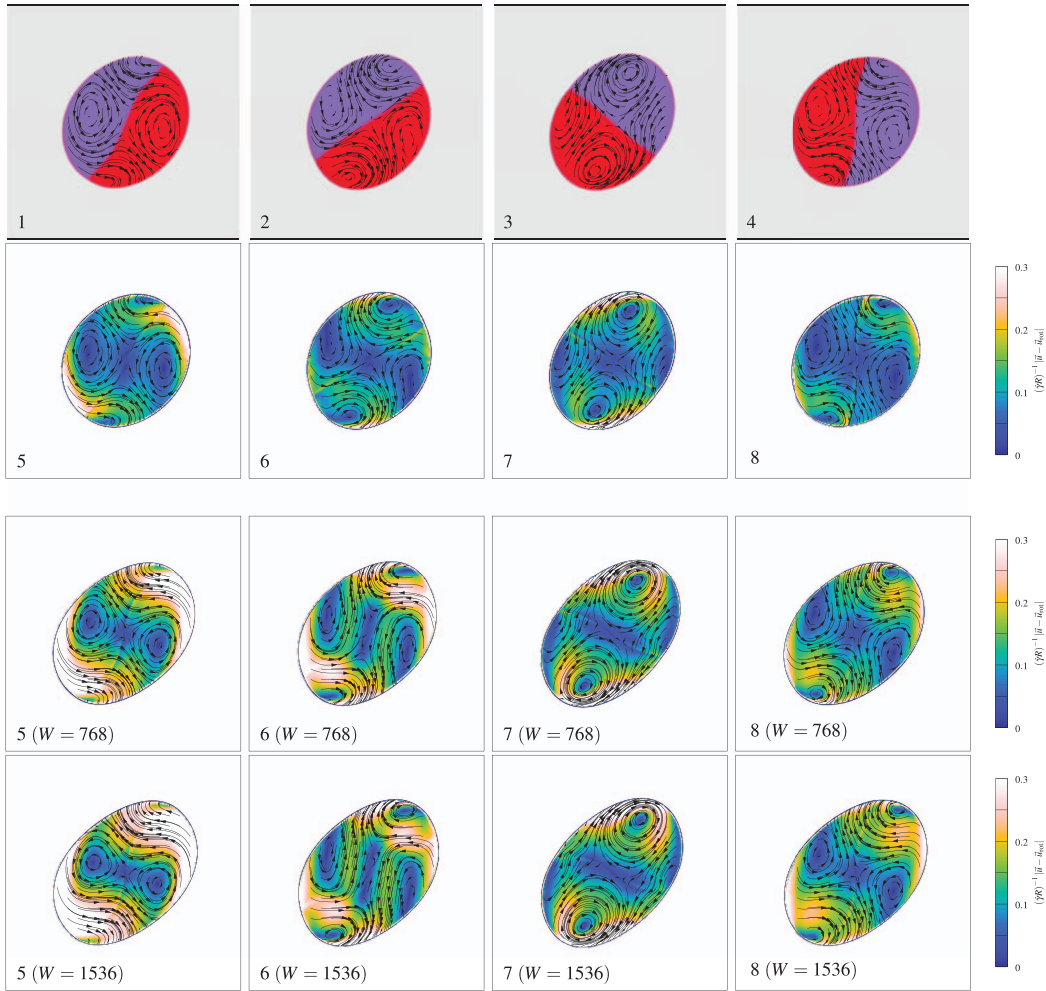


FIG. 12. Streamlines of the internal flow relative to pure rotation ($\vec{u} - \vec{u}_{\text{rot}}$) at the instantaneous rate $\omega(\phi)$ and different droplet orientation angles ϕ . The numbers shown match the labels in Fig. 11. The colour in the upper row identifies the fluid composition; in the lower rows, the colour shows the magnitude of the relative velocity $(\dot{\gamma} R)^{-1} |\vec{u} - \vec{u}_{\text{rot}}|$. The radius R used to scale the velocity magnitude is the radius of the undeformed Janus droplet.

- **Position 2.** All four vortices are present and the rotation rate is halfway between the minimum and maximum rates. After position 2, the two vortices that rotate against the shear direction are no longer present, and the two vortices that rotate with the shear flow grow. The growth continues until position 3.
- **Position 3.** The rotation rate is slowest, and the vortices are largest. In this position, the internal interface is aligned against the applied shear. Fluid in the vortices moves faster than the local speed due to rigid-body rotation in the region near the outer interface and slower near the centre of the droplet. After position 3, the two vortices shrink and the other two form.
- **Position 4.** The two vortices that started forming after position 3 are present, and they rotate against the applied shear. These vortices then grow and the cycle repeats.

Due to symmetry, positions 5–8 are equivalent to positions 1–4. To summarize, the rotation rate is in the upper half of its range when two vortices that rotate against the shear flow are present; the rate is in the lower half when vortices that rotate with the shear flow are present.

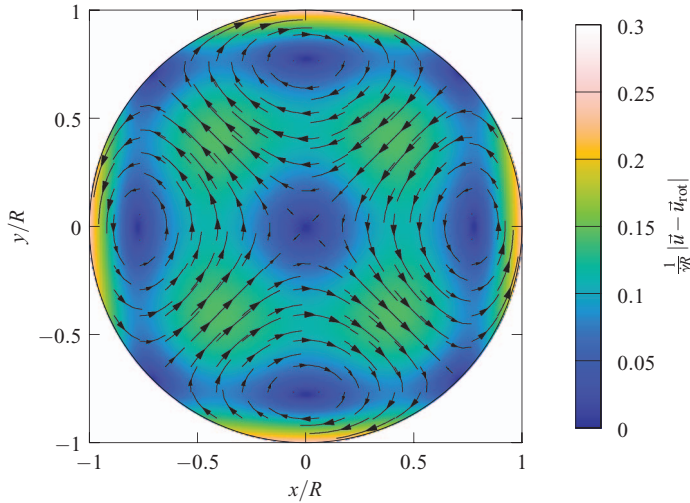


FIG. 13. Streamlines and velocity magnitude (colour) of the internal flow relative to pure rotation ($\vec{u} - \vec{u}_{\text{rot}}$) at the average rate $\omega = \frac{1}{2}\dot{\gamma}$ for an undeformed drop in Stokes flow.^{25,27,31}

V. CONCLUSIONS

The equilibrium states of Janus droplets in stationary fluid and the rotation of Janus droplets in shear flow were simulated. A force balance model was used to obtain equations for calculating interfacial tension ratios from the equilibrium geometry of a Janus droplet. The inverse problem of determining the equilibrium geometry for known interfacial tensions was also solved. These equations were used to evaluate the use of the two-dimensional Shan-Chen lattice Boltzmann method for simulations of Janus droplets. Excellent agreement was found between the interfacial tensions obtained from the equilibrium geometry and from the Young-Laplace law. Systems with adhering, separated, and engulfed droplets were shown.

Adhering droplets with two different geometries in shear flow were simulated. When the geometry of the Janus droplet is two slightly overlapping circles, the Janus droplet rotates fastest when oriented vertically and slowest when horizontal. While the droplet rotates, its centre of mass oscillates between the shear planes. This first type of Janus droplet rotates at an average rate of 70% the rate of solid cylinders in unconfined shear flow. The average rotation rate increases to 80% as the aspect ratio of the domain increases from 1:1 (width:height) to 6:1. In the second type of Janus droplet, the two portions of the droplet had a nearly semicircular shape. These droplets do not oscillate between the shear planes and rotate at the same average rate as the first type. The amplitude of the fluctuation in the rotation rate is smaller for the second type of droplet, and the orientations for maximum and minimum rotation are also different. The internal flow in the second type of Janus droplet was analyzed by subtracting the rotation of an identically shaped rigid body from the flow field. A four-pole vortex structure was found, and its structure and magnitude are similar to those of the flow in a sheared homogeneous drop. The vortices are present in nearly constant locations (in a stationary frame of reference; the vortex positions do not rotate with the droplets) provided that the inter-droplet interface does not pass through them. The maximum and minimum rotation rates occur when the internal interface passes through two of the vortex positions, leaving only two co-rotating vortices. These simulations of semicircular Janus droplets were performed in square domains with twice the width and height of the droplet's diameter. In simulations with domains that are sufficiently large to approximate horizontally unconfined droplets, the structure of the vortices remains the same, the average rate of rotation decreases to 60% of the rate of a solid cylinder, and the amplitude of the fluctuation in the rotation rate doubles.

Surface tension ratios determine the geometry and consequently the behaviour of Janus droplets in shear. Though spurious currents restrict the parameter range in which physically correct results can be obtained, simulation results with the Shan-Chen method provide insight into the ways that Janus

droplets with different geometries behave in shear flow. To determine the feasible parameter range for Shan-Chen simulations of droplets and emulsions in shear, it is recommended to first perform simulations with high shear speeds (0.1 lattice units, near the upper limit for incompressible flow) and well-resolved droplets ($R > 20$ lattice units). The shear speed may then be decreased until unphysical behaviour occurs when spurious currents and the imposed shear flow have comparable magnitudes. The streamlines of the flow with shear should be compared with the streamlines of the spurious currents in the absence of shear to assess whether the effects of spurious currents are small. Based on the results for single droplets, Janus emulsions are expected to exhibit a rich and complex range of behaviours and therefore rheologies. Further work is needed to study droplets in three-dimensional simulations, reduce spurious currents, and thus expand the range of feasible parameters, and eventually simulate emulsions of Janus droplets and chains.

ACKNOWLEDGMENTS

O.S. thanks NSERC for an Alexander Graham Bell Canada Graduate Scholarship.

- ¹A. Gunde, T. Babadagli, S. Roy, and S. Mitra, "Pore-scale interfacial dynamics and oil-water relative permeabilities of capillary driven counter-current flow in fractured porous media," *J. Petrol. Sci. Eng.* **103**, 106–114 (2013).
- ²F. Boyer, C. Lapuerta, S. Minjeaud, B. Piar, and M. Quintard, "Cahn-Hilliard/Navier-Stokes model for the simulation of three-phase flows," *Transport Porous Med.* **82**, 463–483 (2010).
- ³Ovid, *Fasti*, Vol. 1 (8 AD).
- ⁴P. Hardie, "The Janus episode in Ovid's Fasti," *Materiali e discussioni per l'analisi dei testi classici* **26**, 46–64 (1991).
- ⁵H. Hasinovic, S. E. Friberg, and G. Rong, "A one-step process to a Janus emulsion," *J. Colloid Interf. Sci.* **354**, 424–426 (2011).
- ⁶H. Hasinovic and S. E. Friberg, "One-step inversion process to a Janus emulsion with two mutually insoluble oils," *Langmuir* **27**, 6584–6588 (2011).
- ⁷N. Pannacci, H. Bruus, D. Bartolo, I. Etchart, T. Lockhart, Y. Hennequin, H. Willaime, and P. Tabeling, "Equilibrium and nonequilibrium states in microfluidic double emulsions," *Phys. Rev. Lett.* **101**, 164502 (2008).
- ⁸A. Utada, E. Lorenceau, D. Link, P. Kaplan, H. Stone, and D. Weitz, "Monodisperse double emulsions generated from a microcapillary device," *Science* **308**, 537–541 (2005).
- ⁹D. L. Chen, L. Li, S. Reyes, D. Adamson, and R. Ismagilov, "Using three-phase flow of immiscible liquids to prevent coalescence of droplets in microfluidic channels: Criteria to identify the third liquid and validation with protein crystallization," *Langmuir* **23**, 2255–2260 (2007).
- ¹⁰J. Guzowski, P. Morczyk, S. Jakiela, and P. Garstecki, "The structure and stability of multiple micro-droplets," *Soft Matter* **8**, 7269–7278 (2012).
- ¹¹J. Kim and J. Lowengrub, "Phase field modelling and simulation of three-phase flows," *Interface Free Bound.* **7**, 435–466 (2005).
- ¹²J. Zhang and D. Kwok, "A mean-field free energy lattice Boltzmann model for multicomponent fluids," *Eur. Phys. J. Spec. Top.* **171**, 45–53 (2009).
- ¹³S. Leclaire, M. Reggio, and J.-Y. Trépanier, "Progress and investigation on lattice Boltzmann modeling of multiple immiscible fluids or components with variable density and viscosity ratios," *J. Comput. Phys.* **246**, 318–342 (2013).
- ¹⁴X. Shan and H. Chen, "Lattice Boltzmann model for simulating flows with multiple phases and components," *Phys. Rev. E* **47**, 1815–1820 (1993).
- ¹⁵Q. Kang, D. Zhang, and S. Chen, "Displacement of a three-dimensional immiscible droplet in a duct," *J. Fluid Mech.* **545**, 41–66 (2005).
- ¹⁶S. Torza and S. Mason, "Three-phase interactions in shear and electrical fields," *J. Colloid Interf. Sci.* **33**, 67–83 (1970).
- ¹⁷S. Chen and G. Doolen, "Lattice Boltzmann method for fluid flows," *Annu. Rev. Fluid Mech.* **30**, 329–364 (1998).
- ¹⁸C. Aidun and J. Clausen, "Lattice-Boltzmann method for complex flows," *Annu. Rev. Fluid Mech.* **42**, 439–472 (2010).
- ¹⁹X. Shan and G. Doolen, "Multicomponent lattice-Boltzmann model with interparticle interaction," *J. Stat. Phys.* **81**, 379–393 (1995).
- ²⁰Z. Yang, T. Dinh, R. Nourgaliev, and B. Sehgal, "Numerical investigation of bubble coalescence characteristics under nucleate boiling condition by lattice-Boltzmann model," *Int. J. Therm. Sci.* **39**, 1–17 (2000).
- ²¹V. Pratt, "Direct least-squares fitting of algebraic surfaces," *SIGGRAPH Comput. Graph.* **21**, 145–152 (1987).
- ²²A. Ladd, "Numerical simulations of particulate suspensions via a discretized Boltzmann equation. part 1. theoretical foundation," *J. Fluid Mech.* **271**, 285–309 (1994).
- ²³Q. Zou and X. He, "On pressure and velocity boundary conditions for the lattice Boltzmann BGK model," *Phys. Fluids* **9**, 1591–1598 (1997).
- ²⁴X. Shan, "Analysis and reduction of the spurious current in a class of multiphase lattice Boltzmann models," *Phys. Rev. E* **73**, 047701 (2006).
- ²⁵W. Bartok and S. Mason, "Particle motions in sheared suspensions. VII. Internal circulation in fluid droplets (theoretical)," *J. Colloid. Sci.* **13**, 293–307 (1958).
- ²⁶F. Bretherton, "Slow viscous motion round a cylinder in a simple shear," *J. Fluid Mech.* **12**, 591–613 (1962).

- ²⁷F. Rumscheidt and S. Mason, "Particle motions in sheared suspensions. XI. Internal circulation in fluid droplets (experimental)," *J. Colloid. Sci.* **16**, 210–237 (1961).
- ²⁸A. Nir and A. Acrivos, "On the creeping motion of two arbitrary-sized touching spheres in a linear shear field," *J. Fluid Mech.* **59**, 209–223 (1973).
- ²⁹G. Jeffery, "The motion of ellipsoidal particles immersed in a viscous fluid," *Proc. R. Soc. Londond, Ser. A* **102**, 161–179 (1922).
- ³⁰A. Vananroye, P. Janssen, P. Anderson, P. Van Puyvelde, and P. Moldenaers, "Microconfined equiviscous droplet deformation: Comparison of experimental and numerical results," *Phys. Fluids* **20**, 013101 (2008).
- ³¹G. Taylor, "The viscosity of a fluid containing small drops of another fluid," *Proc. R. Soc. London, Ser. A* **138**, 41–48 (1932).